A 3D SYMMETRIC CELL-CENTERED LAGRANGIAN SCHEME BASED ON A MULTI-DIMENSIONAL MINMOD LIMITER

GABRIEL GEORGES[*], JEROME BREIL[*] AND PIERRE-HENRI MAIRE[†]

[*] Centre Lasers Intenses et Applications (CELIA)
Université Bordeaux 1
351 Cours de la Libération, 33405 Talence, France
e-mail: georges@celia.u-bordeaux1.fr - Web page: http://www.celia.u-bordeaux1.fr

[†] Commissariat a l'energie atomique et aux energie alternatives (CEA/CESTA)
15 Avenue des Sablières CS 60001, 33116 Le Barp cedex, France
Web page: http://www.cea.fr

Key words: Lagrangian Hydrodynamics, Cell-Centered, Mutli-Dimensional, Slope Limiter

Abstract. The gas dynamic equations under the Lagrangian formalism are well adapted to the simulation of multi-material compressible fluid flows such as those encountered in the domain of Inertial Confinement Fusion (ICF). The cell-centered finite volume scheme presented here solves these equations on multi-dimensional unstructured meshes. In this scheme, the node velocity is computed by imposing a momentum balance conservation condition around each node. Both momentum and total energy are globally conserved. The second order extension is based on a piecewise linear reconstruction of the pressure and velocity fields obtained via a least squares procedure. A new slope limiter based on a multi-dimensional extension of the minmod method is developed to ensure the monotonicity. Several academic test cases are studied in order to prove the robustness and the accuracy of the method.

1 INTRODUCTION

The Inertial Confinement Fusion (ICF) is a domain of physics which aims to perform nuclear fusion by heating a deuterium-tritium target with lasers. The compression of an ICF target is a complex flow with strong shock waves and rarefaction waves. The Lagrangian formalism of the Euler equations is well suited to treat this hydrodynamical flow. The Lagrangian feature leads to a natural refinement in the shock zones and a cell relaxation in the rarefaction zones. In particular, it enables to treat complex flows with

reasonable size of mesh.

Different methods can solve these equations [4, 6, 5]. Here we are focused on the finite volume cell-centered schemes in arbitrary dimension [1, 3, 2]. More precisely, we are interested on the second order extension of such Godunov schemes which lies in the linear reconstruction of the pressure and velocity fields. In order to avoid oscillations due to this reconstruction, we present a new limitation procedure based on the 3D extension of the minmod approach. The second order extension in time is assured by a Predictor-Corrector method which is not detailed here.

The paper is structured as follows. Section 2 presents the set of equations used to model the Lagrangian hydrodynamics. In Section 3, a symmetric splitting is proposed for the quadrangular faces of hexahedral cells and the resulting nomenclature is detailed. The scheme and the nodal solver from [2] are constructed in Section 4. Section 5 presents in details the second order extension and the multi-dimensional minmod limiter. Finally, this new limiter is compared to the Barth-Jespersen limiter on different academic test cases in Section 6.

2 GOVERNING EQUATIONS

Let $\Omega(t) \in \mathbb{R}^3$ be a domain of fluid and $\Sigma(t)$ its boundary, then for a fluid of density ρ, velocity $\boldsymbol{v}$, pressure P and total energy E, the gas dynamics equations under its Lagrangian form write

$$\begin{cases} \dfrac{d}{dt} \displaystyle\int_{\Omega(t)} \rho \, \mathrm{d}\omega = 0, \\[2mm] \dfrac{d}{dt} \displaystyle\int_{\Omega(t)} \rho \boldsymbol{v} \, \mathrm{d}\omega + \displaystyle\int_{\Sigma(t)} P\boldsymbol{n} \, \mathrm{d}\sigma = \boldsymbol{0}, \\[2mm] \dfrac{d}{dt} \displaystyle\int_{\Omega(t)} \rho E \, \mathrm{d}\omega + \displaystyle\int_{\Sigma(t)} P\boldsymbol{v} \cdot \boldsymbol{n} \, \mathrm{d}\sigma = 0, \end{cases} \tag{1}$$

where $\boldsymbol{n}$ is the unit outward normal of $\Sigma(t)$ and the equations correspond respectively to the mass conservation, the momentum conservation and the total energy conservation.

Under a Lagrangian formalism, the Geometric Conservation Law (GCL) is added to ensure the volume conservation

$$\frac{d}{dt} \int_{\Omega(t)} \mathrm{d}\omega - \int_{\Sigma(t)} \boldsymbol{v} \cdot \boldsymbol{n} \, \mathrm{d}\sigma = 0, \tag{2}$$

and the trajectory equation for a point $\boldsymbol{X} \in \Omega(t)$ writes

$$\begin{cases} \dfrac{d\boldsymbol{X}}{dt} = \boldsymbol{v}, \\[2mm] \boldsymbol{X}(t = 0) = X_0. \end{cases} \tag{3}$$
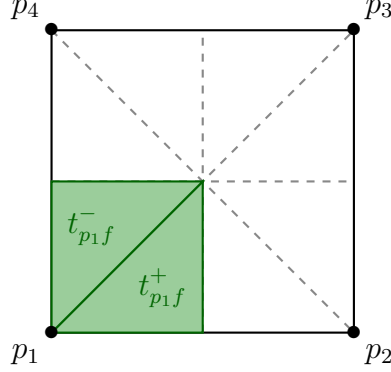
Figure 1: Geometric splitting of a quadrangular face f based on the face barycenter and the edge midpoints, creating triangles $t_{p_i f}^+$ and $t_{p_i f}^-$ around the node p_i.

The following thermodynamics relations are chosen as a closure, they define the internal energy ε and the pressure P such as

$$\begin{cases} \varepsilon = E - \dfrac{1}{2}||\boldsymbol{v}||^2, \\ P = (\gamma - 1)\rho\varepsilon, \end{cases} \tag{4}$$

where γ is the polytropic index of the gas.

3 NOTATIONS AND FACE SPLITTING

The spatial domain $\Omega(t)$ is discretized in N_c non-overlapping polyhedrons denoted Ω_c such that $\Omega(t) = \bigcup_c \Omega_c$. Knowing that k points have no reason to be coplanar in a 3D geometry as soon as $k > 3$, a special treatment is required for the quadrangular faces [2, 3]. Here such faces are split as shown on Figure 1 by using the face barycenter and the edges midpoints. This provides a systematic and symmetric splitting for quadrangular faces.

This splitting enables to define a unique area S_{pf}^+ and an outward normal $\boldsymbol{n}_{pf}^+$ for the triangle t_{pf}^+ (respectively S_{pf}^- and $\boldsymbol{n}_{pf}^-$ for the triangle t_{pf}^-). From now the exponent $\pm$ underlines that both triangles t_{pf}^+ and t_{pf}^- have to be considered. The following topological sets are defined :

- $\mathcal{P}(c)$ is the set of nodes p of cell c,

- $\mathcal{F}(c)$ is the set of faces f of cell c,

- $\mathcal{C}(p)$ is the set of cells c sharing node p,

- $\mathcal{C}(c)$ is the set of cells c sharing a face f with cell c.
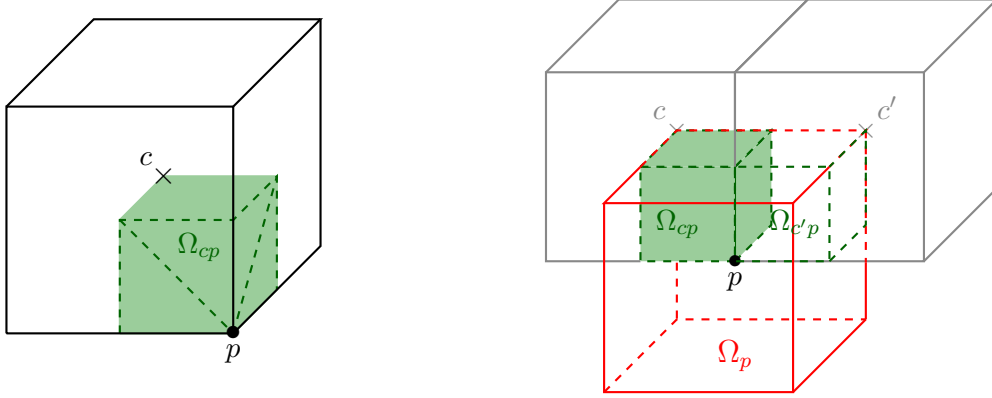
Figure 2: Representation of the sub-cell Ω_{cp} (left) and the dual-cell Ω_p (right) for the simple case of hexahedral cells with square faces.

Lets the sub-cell Ω_{cp} be the cell connecting the cell centroid c to the triangles $t_{pf}^{\pm}$ around the node p, and the dual-cell Ω_p as the union of the sub-cells Ω_{cp} around the node p (see Figure 2), then the following relations can be written

$$
\begin{cases}
\Omega_p = \displaystyle\bigcup_{c \in \mathcal{C}(p)} \Omega_{cp}, \\[2ex]
\Omega_c = \displaystyle\bigcup_{p \in \mathcal{P}(c)} \Omega_{cp}.
\end{cases}
\tag{5}
$$

The following sets are defined for the sub-cells :

- $\mathcal{C}_{cp}(p)$ is the set of sub-cells sharing point p,

- $\mathcal{F}_{cp}(p)$ is the set of faces of the sub-cell Ω_{cp} sharing point p.

4 SCHEME CONSTRUCTION

4.1 Equation discretization

Under a Lagrangian formalism, the mass conservation equation in (1) writes straight-forward

$$
\frac{dm_c}{dt} = 0 \quad \text{where} \quad m_c = \int_{\Omega_c} \rho \, d\omega.
\tag{6}
$$

The mass is constant in each cell, thus solving the GCL is not necessary. The cell volume V_c^{n+1} is deduced from the geometry at time t^{n+1} and the cell density is thus computed thanks to

$$
\rho_c^{n+1} = \frac{V_c^{n+1}}{m_c}
\tag{7}
$$

Mass averaged values φ_c are defined over cell Ω_c for each physical variable $\varphi = \rho, \boldsymbol{v}, E, P$ or ε by the relation

$$\varphi_c = \frac{1}{m_c} \int_{\Omega_c} \rho\varphi \, d\omega. \tag{8}$$

Thus the system (1) writes for a cell Ω_c

$$\begin{cases} m_c \dfrac{d\boldsymbol{v_c}}{dt} + \displaystyle\sum_{f \in \mathcal{F}(c)} S_{pf}^{\pm} P_{pcf}^{\pm} \boldsymbol{n_{pf}^{\pm}} = \boldsymbol{0}, \\[3mm] m_c \dfrac{dE_c}{dt} + \displaystyle\sum_{f \in \mathcal{F}(c)} S_{pf}^{\pm} \left(P_{pcf} \boldsymbol{v_{pf}} \right)^{\pm} \cdot \boldsymbol{n_{pf}^{\pm}} = 0, \end{cases} \tag{9}$$

where the velocity $\boldsymbol{v_{pf}^{\pm}}$ and the pressure $P_{pcf}^{\pm}$ on the triangle $t_{pf}^{\pm}$ are defined such that

$$\begin{cases} \boldsymbol{v_{pf}^{\pm}} = \dfrac{1}{S_{pf}^{\pm}} \displaystyle\int_{t_{pf}^{\pm}} \boldsymbol{v} \, d\sigma = \boldsymbol{v_p}, \\[3mm] P_{pcf}^{\pm} = \dfrac{1}{S_{pf}^{\pm}} \displaystyle\int_{t_{pf}^{\pm}} P \, d\sigma. \end{cases} \tag{10}$$

Concerning the total energy flux through the triangle $t_{pf}^{\pm}$, the following simplifying assumption is made

$$\left(P_{pcf} \boldsymbol{v_p} \right)^{\pm} = \frac{1}{S_{pf}^{\pm}} \int_{t_{pf}^{\pm}} P\boldsymbol{v} \, d\sigma = P_{pcf}^{\pm} \boldsymbol{v_p}. \tag{11}$$

4.2 Nodal fluxes

In order to construct a Godunov-type scheme, the pressure flux $P_{pcf}^{\pm}$ is defined as the Riemann invariant along the direction $\boldsymbol{n_{pf}^{\pm}}$ as in [1]

$$P_{pcf}^{\pm} - P_c = \rho_c a_c \left(\boldsymbol{v_c} - \boldsymbol{v_p} \right) \cdot \boldsymbol{n_{pf}^{\pm}}, \tag{12}$$

where a_c is the speed of sound in the cell defined by

$$a_c = \sqrt{\frac{\gamma_c P_c}{\rho_c}}. \tag{13}$$

Following the work of [2], the node velocity is computed by imposing a local momentum balance conservation condition around node p. The node velocity $\boldsymbol{v_p}$ writes

$$\boldsymbol{v_p} = \overline{\overline{M}}_p^{-1} \cdot \sum_{c \in \mathcal{C}_{cp}(p)} \sum_{f \in \mathcal{F}_{cp}(p)} \left[S_{pf}^{\pm} P_c \boldsymbol{n_{pf}^{\pm}} + \overline{\overline{M}}_{pc} \cdot \boldsymbol{v_c} \right], \tag{14}$$

where

$$\overline{\overline{M}}_p = \sum_{c \in \mathcal{C}_{cp}(p)} \sum_{f \in \mathcal{F}_{cp}(p)} \overline{\overline{M}}_{pc}, \tag{15}$$

and

$$\overline{\overline{M}}_{pc} = S_{pf}^{\pm} \rho_c a_c \left(\boldsymbol{n_{pf}^{\pm}} \otimes \boldsymbol{n_{pf}^{\pm}} \right). \tag{16}$$

5 SECOND ORDER EXTENSION

5.1 Linear reconstruction of the velocity and pressure fields

The second order extension of such Godunov-type schemes lies in the linear reconstruction of the pressure and velocity fields in each cell Ω_c. This enables to calculate more accurate fluxes for the determination of the node velocity. Those linear reconstructions are written

$$\begin{cases} \tilde{P}_c(\boldsymbol{X}) = \bar{P}_c + \nabla P_c.(\boldsymbol{X} - \boldsymbol{X_c}), \\ \tilde{\boldsymbol{v_c}}(\boldsymbol{X}) = \bar{\boldsymbol{v_c}} + \overline{\overline{\nabla}}\boldsymbol{v_c}.(\boldsymbol{X} - \boldsymbol{X_c}), \end{cases} \tag{17}$$

where $\tilde{P}_c(\boldsymbol{X})$ and $\tilde{\boldsymbol{v_c}}(\boldsymbol{X})$ are the pressure and the velocity reconstructed at point $\boldsymbol{X} \in \Omega_c$. $\bar{P}_c$ and $\bar{\boldsymbol{v_c}}$ are the mean values in cell c and $\boldsymbol{X_c}$ the cell centroid. This centroid is numerically evaluated following the work of [7] and defined as

$$\boldsymbol{X_c} = \frac{1}{V_c} \int_{\Omega_c} \boldsymbol{X} \, \mathrm{d}\omega. \tag{18}$$

Finally, the gradient ∇P_c and tensor gradient $\overline{\overline{\nabla}}\boldsymbol{v_c}$ are evaluated in the cell using a least squares method [2].

The Total Variation Diminishing (TVD) criterion as to be applied on these reconstructions, it requires a monotonic reconstruction in order to avoid oscillations. For a scalar variable $\varphi = P$ or $||\boldsymbol{v}||$, it writes

$$\min_{c' \in \mathcal{C}(c)} \bar{\varphi}_{c'} \leq \tilde{\varphi}_c(\boldsymbol{X_p}) \leq \max_{c' \in \mathcal{C}(c)} \bar{\varphi}_{c'}, \qquad \forall p \in \mathcal{P}(c), \tag{19}$$

where $\boldsymbol{X_p}$ are the node coordinates.

5.2 The Barth-Jespersen limiter

The classical Barth-Jespersen limiter consists in applying a scalar $\phi_c \in [0,1]$ on the gradient. This scalar is defined as

$$\phi_c = \min_{p \in \mathcal{P}(c)} (1, \phi_{c,p}), \quad \text{where} \quad \phi_{c,p} = \begin{cases} \dfrac{\bar{\varphi}_{c'}^{max} - \bar{\varphi}_c}{\tilde{\varphi}_c(\boldsymbol{X_p}) - \bar{\varphi}_c}, & \text{if } \tilde{\varphi}_c(\boldsymbol{X_p}) > \bar{\varphi}_c, \\ \dfrac{\bar{\varphi}_{c'}^{min} - \bar{\varphi}_c}{\tilde{\varphi}_c(\boldsymbol{X_p}) - \bar{\varphi}_c}, & \text{if } \tilde{\varphi}_c(\boldsymbol{X_p}) < \bar{\varphi}_c, \\ 1, & \text{if } \tilde{\varphi}_c(\boldsymbol{X_p}) = \bar{\varphi}_c, \end{cases} \tag{20}$$

where $\bar{\varphi}_{c'}^{max} = \max_{c' \in \mathcal{C}(c)} \bar{\varphi}_{c'}$ and $\bar{\varphi}_{c'}^{min} = \min_{c' \in \mathcal{C}(c)} \bar{\varphi}_{c'}$.

Finally, the limited extrapolated value at point $\boldsymbol{X}$ writes

$$\tilde{\varphi}_c^{barth}(\boldsymbol{X}) = \bar{\varphi}_c + \phi_c \boldsymbol{\nabla}\varphi_c \cdot (\boldsymbol{X} - \boldsymbol{X_c}), \qquad \forall \boldsymbol{X} \in \Omega_c. \tag{21}$$

It is shown on Figure 4 that this method can leads to residual oscillations.
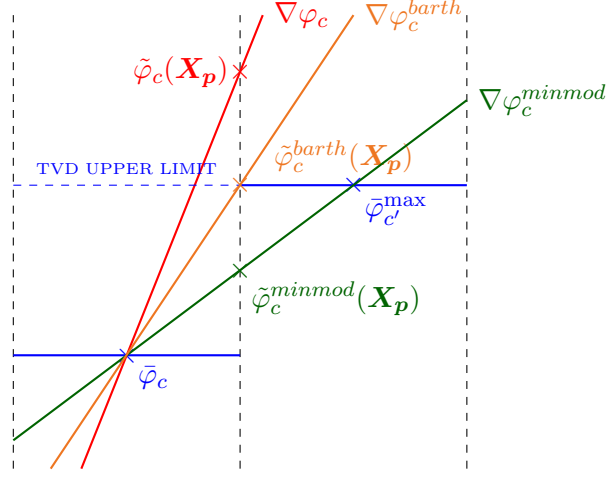
Figure 3: Comparison between the Barth-Jespersen and the multi-dimensional minmod limiter. The non-limited gradient issued from the least squares method ($\nabla\varphi_c$) implies an extrapolated value above the TVD limit. The *barth* limited gradients ($\nabla\varphi_c^{barth}$) projects this extrapolated value on the TVD limit while the *minmod* ($\nabla\varphi_c^{minmod}$) projects this value under the TVD limit.

5.3 The multi-dimensional minmod limiter

In order to avoid any oscillations, a new limitation procedure is introduced. One has to remark that the Barth-Jespersen limiter projects the extrapolated values exactly on the TVD limit, thus the idea is to project these values under the TVD limit (see Figure 3).

In order to construct a limited gradient in the cell Ω_c, nodal gradients are projected on a certain direction. The nodal gradients are calculated for each node $p \in \mathcal{P}(c)$ by a least squares method based on the cells $c \in \mathcal{C}(p)$. And the aforesaid direction is denoted $\boldsymbol{d_c^P}$ for the pressure limitation and $\boldsymbol{d_c^v}$ for the velocity limitation.

In the case of the pressure limitation, the direction $\boldsymbol{d_c^P}$ is defined as the direction vector of the pressure gradient in the cell and writes

$$\boldsymbol{d_c^P} = \frac{\boldsymbol{\nabla P_c}}{||\boldsymbol{\nabla P_c}||}. \tag{22}$$

The nodal gradients are then projected on this direction

$$\nabla P_{p,c}^{proj} = \boldsymbol{\nabla P_{p,c}} \cdot \boldsymbol{d_c^P}, \quad p \in \mathcal{P}(c). \tag{23}$$

The final limited gradient is chosen as

$$\boldsymbol{\nabla P_c^{minmod}} = minmod(\nabla P_{p,c}^{proj})\boldsymbol{d_c^P}, \tag{24}$$

where

$$minmod(\lambda_i)_{i=1,n} = \min(0, \max_{i \in [1,n]}(\lambda_i)) + \max(0, \min_{i \in [1,n]}(\lambda_i)), \quad \forall \{\lambda_1, ..., \lambda_n\} \in \mathbb{R}^n. \quad (25)$$

In the case of the velocity limitation, the direction $\boldsymbol{d_c^v}$ is chosen as being the flow direction in the cell c such that

$$\boldsymbol{d_c^v} = \frac{\boldsymbol{v_c}}{||\boldsymbol{v_c}||}. \quad (26)$$

The nodal gradients are projected on this direction

$$\nabla v_{p,c}^{proj} = \left(\overline{\overline{\boldsymbol{\nabla}}} \boldsymbol{v_{p,c}} \cdot \boldsymbol{d_c^v}\right) \cdot \boldsymbol{d_c^v}, \quad (27)$$

and the final limited velocity gradient is defined as

$$\boldsymbol{\nabla v_c^{minmod}} = minmod(\nabla v_{p,c}^{proj}) \boldsymbol{d_c^v}. \quad (28)$$

This method enables to reconstruct a velocity field only in the direction $\boldsymbol{d_c^v}$ which writes

$$\tilde{v}_c(\boldsymbol{X_p}) = \left(||\boldsymbol{v_c}|| + \boldsymbol{\nabla v_c^{lim}} \cdot (\boldsymbol{X_p} - \boldsymbol{X_c})\right) \boldsymbol{d_c^v}.$$

6 VALIDATION ON TEST CASES

6.1 Sod test case

The sod test case considers a domain $\Omega(0) = (x, y, z) \in [0; 1]^3$ split in the middle by the plane $x = 0.5$. Symmetric boundary conditions are applied on each boundary face of the domain which is filled with a perfect diatomic gas such as

$$\begin{cases} (\rho_l, P_l, \boldsymbol{v_l}) = (1.0, 1.0, \boldsymbol{0}), & \text{for } x \leq 0.5, \\ (\rho_r, P_r, \boldsymbol{v_r}) = (0.125, 0.1, \boldsymbol{0}), & \text{for } x \geq 0.5, \\ \gamma_l = \gamma_r = \dfrac{7}{5}. \end{cases} \quad (29)$$

This test case is interesting since it presents a shock wave and a contact discontinuity which propagate to the right and a rarefaction wave propagating to the left.
The density along the x axis shown on Figure 4 shows the good accordance between the numerical solutions and the analytical solution. One can observe that the second order numerical solution oscillates around the shock zone with the Barth-Jespersen limiter while it stays monotonic with the multi-dimensional minmod limiter.
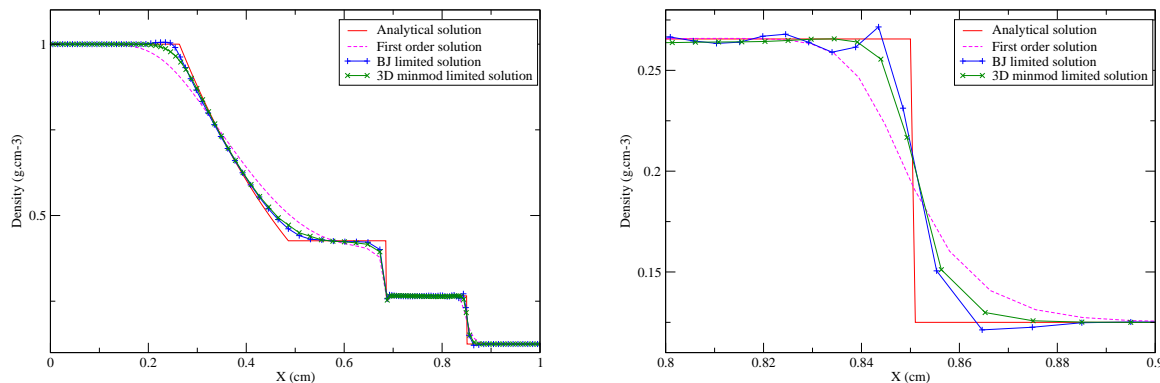
Figure 4: Comparison between the first and the second-order density solutions at time $t = 0.2\ s$ along the x axis for the Sod test case on a $100 \times 10 \times 10$ mesh (left). Both the 3D minmod and the Barth-Jespersen limiters are plotted. - Zoom around the shock zone (right).

6.2 Noh test case

The Noh problem models the implosion of a domain $\Omega(0) = (x, y, z) \in [0; 1]^3$ filled with a perfect monoatomic gas such as

$$
\begin{cases}
(\rho^0, P^0, \boldsymbol{v^0}) = (1, 10^{-6}, -\boldsymbol{e_r}), \\
\gamma = \dfrac{5}{3},
\end{cases}
\tag{30}
$$

where $\boldsymbol{e_r}$ is the radial vector. Symmetry conditions are applied on the boundaries holding the origin $\boldsymbol{X_o} = \boldsymbol{0}$, the others are pressure conditions with $\mathcal{P}_b = 10^{-6}\ dyne.cm^{-2}$. The final time for this implosion is set to $t = 0.6\ s$.

This test case is interesting for studying the scheme symmetry and ability to handle a strong shock wave. The comparison between the second order radial densities obtained with the Barth-Jespersen and the 3D minmod limiters is presented on Figure 6. It is shown that the multi-dimensional minmod limiter enables to recover a good stability around the shock.

6.3 Saltzmann test case

The Saltzmann test case simulates the propagation of an plane shock created by a piston in a domain $\Omega(0) = (x, y, z) \in [0, 1] \times [0, 0.1] \times [0, 0.1]$ filled with a monoatomic gas such as

$$
\begin{cases}
(\rho^0, P^0, \boldsymbol{v^0}) = (1, 10^{-6}, \boldsymbol{0}), \\
\gamma = \dfrac{5}{3}.
\end{cases}
\tag{31}
$$

The piston is modeled by a velocity condition $\mathcal{V}_b = -1\ cm.s^{-1}$ on the initial plane $x = 0$. The other boundaries are symmetry conditions. This test case enables to experience the
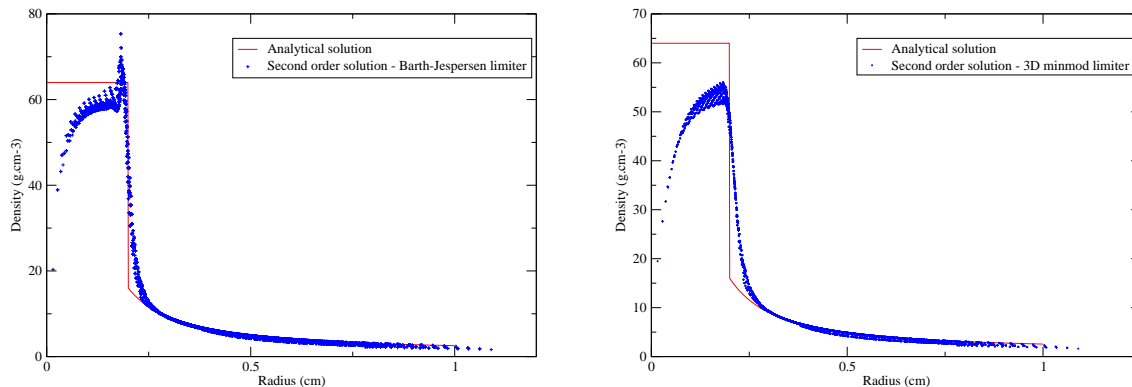
Figure 5: Radial density at time $t = 0.6 \ s$ for the Noh problem on a cubical mesh with $20 \times 20 \times 20$ cells, comparison between the Barth-Jespersen (left) and the 3D minmod limiters (right).
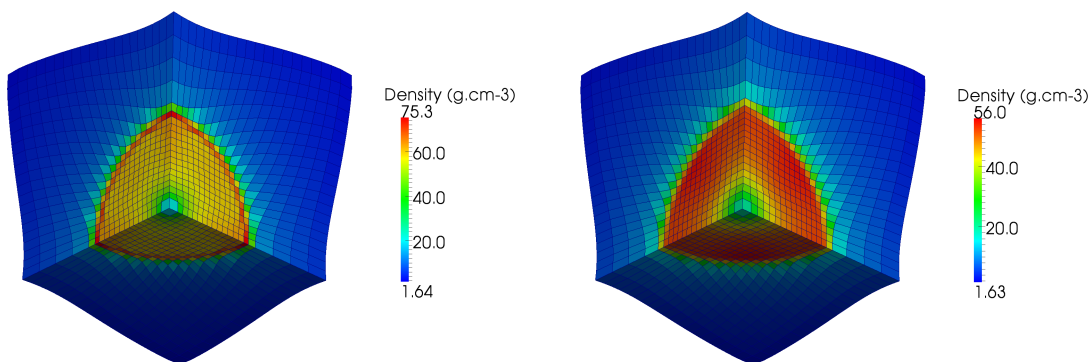
Figure 6: 3D density field at time $t = 0.6 \ s$ for the Noh problem on a cubical mesh with $20 \times 20 \times 20$ cells, comparison between the Barth-Jespersen (left) and the 3D minmod limiters (right).

scheme stability on a 3D skewed mesh such as

$$
\begin{cases}
\tilde{x} = x + (0.1 - z)(1 - 20y)sin(x\pi), & \text{if} \quad 0 \leq y \leq 0.05, \\
\tilde{x} = x + z(20y - 1)sin(x\pi), & \text{if} \quad 0.05 \leq y \leq 0.1, \\
\tilde{y} = y, \\
\tilde{z} = z.
\end{cases}
\tag{32}
$$

The density fields at final times $t = 0.7 \ s$ shows the good stability of the multi-dimensional minmod limiter (see Figure 7). Indeed, one can observe oscillations around the shock zone on the left-hand side figure. Moreover, a sliding of the cells is observable on the 3D density field with the usual limiter which does not occur with the new limiter (see Figure 8).

10
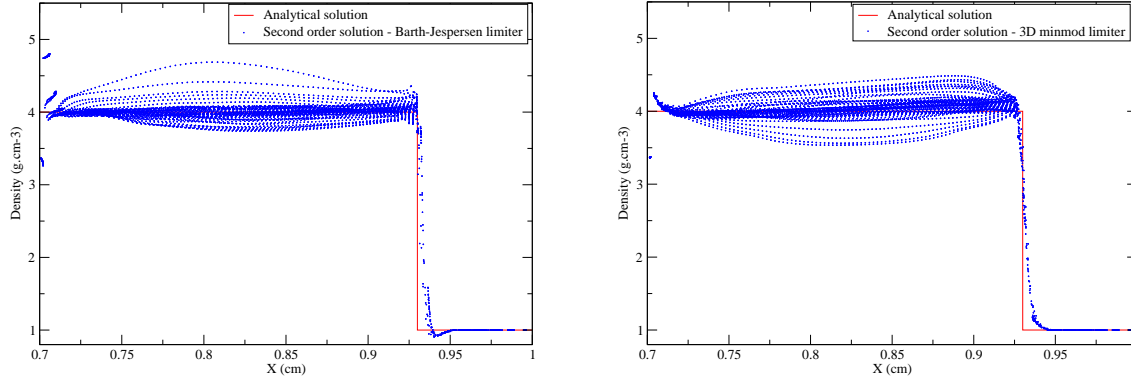
Figure 7: Density on the x axis for the Saltzmann test case at final times $t = 0.7$ s on a $100 \times 10 \times 10$ mesh, comparison between the Barth-Jespersen (left) and the 3D minmod (right) limiters.
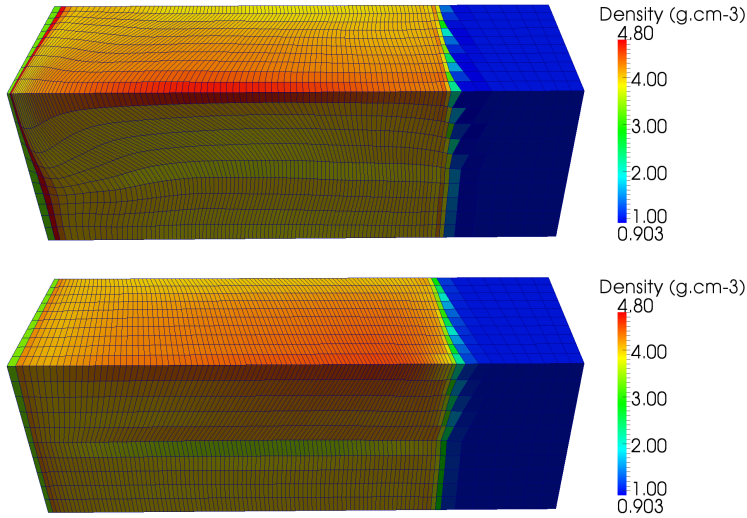
Figure 8: 3D density field for the Saltzmann test case at final times $t = 0.7$ s on a $100 \times 10 \times 10$ mesh, comparison between the Barth-Jespersen (top) and the 3D minmod (bottom) limiters.

7   CONCLUSION

In this paper, we have presented a slope limiter based on a multi-dimensional minmod approach. This method has been applied to a multi-dimensional second order cell-centered Lagrangian scheme for solving the gas dynamics equations. This nodal solver is taken from [2] and is the 3D extension of the one presented in [1]. A symmetric splitting for the quadrangular faces of hexahedral cells is proposed in order to conserve the flow symmetry. The stability and accuracy of this new limiter is tested on several academic test cases and compared to the usual Barth-Jespersen limiter. This new limiter shows a good stability on these difficult problems and enables to avoid oscillations.

11

As a future work, the implementation of an ALE method is planed in order to improve the scheme stability and ability to treat flows with strong distortions and shearing.

REFERENCES

[1] P.-H. Maire, R. Abgrall, J. Breil and J. Ovadia, A cell-centered Lagrangian scheme for two-dimensional compressible flows problems. *SIAM Journal on Scientific Computing.* (2007) **29**:1781–1624.

[2] P.-H. Maire and B. Nkonga, Multi-scale Godunov-type method for cell-centered discrete Lagrangian hydrodynamics. *Journal of Computational Physics.* (2009) **228**:799–821.

[3] G. Carré, S. Del Pino, B. Després and E. Labourasse, A cell-centered Lagrangian hydrodynamics scheme on general unstructured meshes in arbitrary dimension. *Journal of Computational Physics.* (2009) **228**:5160–5183.

[4] V. A. Dobrev, T. V. Kolev and R. N. Rieben, High order curvilinear finite elements for elastic-plastic Lagrangian dynamics. *Journal of Computational Physics.* (2014) **257**:1062–1080.

[5] G. Scovazzi, Lagrangian shock hydrodynamics on tetrahedral meshes: A stable and accurate variational multiscale approach. *Journal of Computational Physics.* (2012) **231**:8029–8069.

[6] R. Loubre, P.-H. Maire and P. Vachal, 3D staggered Lagrangian hydrodynamics scheme with cell-centered Riemann solver-based artificial viscosity. *International Journal for Numerical Methods in Fluids* (2013) **72**:22–42.

[7] B. Mirtich, Fast and Accurate Computation of Polyhedral Mass Properties. *Journal of Graphics Tools* (1996) **1**:31–50.